Applied Catalysis B: Environmental 301 (2022) 120801

Contents lists available at ScienceDirect

Applied Catalysis B: Environmental

journal homepage: www.elsevier.com/locate/apcatb

Catalyst design to direct high-octane gasoline fuel properties for improved engine efficiency

Connor P. Nash [a], Daniel P. Dupuis [a], Anurag Kumar [a], Carrie A. Farberow [a], Anh T. To [a], Ce Yang [b], Evan C. Wegener [b], Jeffrey T. Miller [c], Kinga A. Unocic [d], Earl Christensen [a], Jesse E. Hensley [a], Joshua A. Schaidle [a], Susan E. Habas [a,*], Daniel A. Ruddy [a,*]

[a] Catalytic Carbon Transformation & Scale-up Center, National Renewable Energy Laboratory, Golden, CO 80401, USA
[b] Chemical Sciences and Engineering Division, Argonne National Laboratory, Lemont, IL 60439, USA
[c] School of Chemical Engineering, Purdue University, West Lafayette, IN 47907, USA
[d] Center for Nanophase Materials Science, Oak Ridge National Laboratory, Oak Ridge, TN 37830, USA

ARTICLE INFO

Keywords:
High octane gasoline
Engine efficiency
Dehydrogenation
Paraffin/olefin ratio
Cu/BEA zeolite

ABSTRACT

The paraffin-to-olefin (P/O) ratio in gasoline fuel is a critical metric affecting fuel properties and engine efficiency. In the conversion of dimethyl ether (DME) to high-octane hydrocarbons over BEA zeolite catalysts, the P/O ratio can be controlled through catalyst design. Here, we report bimetallic catalysts that balance the net hydrogenation and dehydrogenation activity during DME homologation. The Cu-Zn/BEA catalyst exhibited greater relative dehydrogenation activity attributed to higher ionic site density, resulting in a lower P/O ratio (6.6) versus the benchmark Cu/BEA (9.4). The Cu-Ni/BEA catalyst exhibited increased hydrogenation due to reduced Ni species, resulting in a higher P/O ratio (19). The product fuel properties were estimated with an efficiency merit function and compared against finished gasolines and a typical alkylate blendstock. Merit values for the hydrocarbon product from all three BEA catalysts exceeded those of the comparison fuels (0–5.3), with the product from Cu-Zn/BEA exhibiting the highest merit value (9.7).

1. Introduction

The transportation sector accounts for 70% of U.S. petroleum consumption, and a corresponding 35% of total U.S. CO_2 emissions [1,2]. Despite the advent of electric vehicles, motor gasoline is expected to constitute 56% of the sector's total energy consumption in 2050 [3]. Thus, the challenge remains to improve gasoline fuel economy and develop economical pathways to incorporate renewable carbon. Advancements in the conversion of methanol and/or dimethyl ether (DME) to high-octane gasoline (HOG) over BEA zeolite catalysts can enable economical utilization of renewable and waste carbon (e.g., DME produced from biomass, municipal solid waste, or bio-gas) in a high-value hydrocarbon fuel product, with a modeled 84% reduction in greenhouse gas (GHG) emissions compared to a petroleum gasoline benchmark [4–9]. The HOG product is comprised of C_{5-8} branched paraffins and olefins, and is especially rich in 2,2,3-trimethylbutane (also called triptane) which has a research octane number (RON) of 112.8 and motor octane number (MON) of 101.3 [5,10]. The HOG fuel properties resemble those of a refinery alkylate stream, which is used as a blendstock to increase gasoline octane rating and is among the most valuable hydrocarbon products in a refinery. Due to these alkylate-like fuel properties, the HOG product is directly responsive to the current demand-driven market for octane in gasoline, and it has no inherent blend limit [11]. Catalyst development research from our laboratory recently demonstrated that a Cu-modified H-form BEA zeolite (Cu/BEA) catalyst out-performs the parent BEA in activity, lifetime, regenerability, and overall HOG yield, resulting in a 35% reduction to modeled conversion cost at relevant production scale [12–14]. Thus, this process holds the potential to provide a renewable and sustainable fuel product with reduced GHG emissions and improved fuel properties, meeting two important market needs, while utilizing an earth-abundant, relatively inexpensive (i.e., non-precious metal), and scalable zeolite catalyst.

The conversion of DME with co-fed H_2 over Cu/BEA results in H-incorporation in the HOG product due to hydrogenation activity of metallic Cu species, and a corresponding shift in the paraffin-to-olefin product ratio (P/O) towards paraffins [12]. To understand the

* Corresponding authors at: Catalytic Carbon Transformation & Scale-up Center, National Renewable Energy Laboratory, Golden, CO 80401, USA
E-mail addresses: Susan.Habas@nrel.gov (S.E. Habas), Dan.Ruddy@nrel.gov (D.A. Ruddy).

https://doi.org/10.1016/j.apcatb.2021.120801
Received 12 August 2021; Received in revised form 24 September 2021; Accepted 5 October 2021
Available online 9 October 2021

importance of the fuel P/O ratio, a simplified explanation of the fuel-engine relationship is presented here. The P/O ratio is a critical metric because it affects the fuel properties and thus engine efficiency. The principal fuel properties affecting engine performance, namely RON, MON, and sensitivity (S = RON – MON), are influenced by the paraffin and olefin content [15]. These properties determine whether the hydrocarbon mixture is suitable for automotive applications, where common fuels have RON > MON, that is, S > 0. Traditionally, the goal has been to produce fuels with high RON and high MON. However, it was recently demonstrated that next-generation strategies to increase engine efficiency (e.g., higher compression ratio, advanced spark timing, turbocharging) are facilitated with higher RON and higher S fuels [16–18].

A predictive metric proposed by Kalghatgi is the octane index (OI), defined by Eq. 1:

$$OI = RON - K * S \quad (1)$$

where K is an experimentally derived constant that is dependent on engine design and operating conditions [16]. Traditionally, K = 0.5 has been used in the U.S. However, modern engines (i.e., after 1995) operating with a higher compression ratio and lower engine speed are more prone to knocking, and subsequently, the value of K becomes negative (i.e., K = –1.25 for modern engines equipped with knock sensors) [16,17,19]. Considering the K value of –1.25 in Eq. 1, the octane index increases with a fuel having high RON and high S (i.e., low MON).

An extension to Eq. 1, the gasoline efficiency merit function, further contextualizes the importance of high RON and high S fuels [19]. The function considers many fuel properties, including RON, MON, S, heat of vaporization, flame speed, lower heating value, air-fuel ratio, and particulate matter index. When comparing gasoline-range hydrocarbon fuels and blendstocks, which is the focus of this report, RON and S are the dominant factors in the merit value. Eq. 2 defines a simplified efficiency merit function for comparison of hydrocarbon mixtures, where the contributing factors outside of RON and S were assumed constant to regular gasoline.

$$Merit = \frac{(RON_{mix} - 91) + 1.25 * (S_{mix} - 8)}{1.6} \quad (2)$$

The terms RON_{mix} and S_{mix} refer to the properties of the fuel mixture, and the K-value of –1.25 was inserted [19]. The normalization by a factor of 1.6 is used to equate the merit function value to the expected percentage increase in engine efficiency, meaning an absolute increase in OI by 1.6 leads to an estimated efficiency increase of 1%. Thus, the merit function quantifies the relative efficiency for a gasoline fuel in a spark-ignition engine compared to Regular-E10 gasoline, which corresponds to Merit = 0. Positive merit values indicate enhanced efficiency and negative values indicate reduced efficiency relative to Regular-E10 gasoline.

The pure-component RON and MON values for representative C_{5-8} species in the HOG product are given in Table 1. For branched paraffins, both the RON and MON values are high (> 90), corresponding to low S values of 2–6. The outlier is triptane, having a particularly high RON, giving a higher S of 11.5. RON values for branched olefins are similarly high (> 90) but MON values are significantly lower (77−83), leading to higher S values. Ghosh et al. developed a model to predict the RON and MON of gasoline-range hydrocarbon mixtures based on their individual RON and MON values, and included factors to account for non-linear blending effects [10]. The fuel properties of paraffins tend to blend linearly, and thus, a fuel consisting of only branched paraffins has a high RON and MON and a relatively low S value. Such a fuel is not advantageous for modern spark-ignition engines in the context of OI with a negative K value. For a mixture of paraffins and olefins, olefins affect the modeled MON value strongly and non-linearly. The resulting multi-component fuel will have a comparably high RON to the paraffin-only fuel, but a lower MON value (i.e., greater S value), leading to an increased OI and merit value (when K < 0). This conceptual analysis shows that the P/O ratio in the HOG hydrocarbon mixture is a key driver of the fuel properties.

Table 1
RON, MON, and S values for representative C_{5-8} components of the HOG product. Values from Ghosh et al. [10].

Paraffins				Olefins			
	RON	MON	S		RON	MON	S
Iso-pentane	92	90	2	Iso-pentenes	103	82	21
Dimethyl-C_6	99	94	5	Iso-hexenes	100	83	17
Dimethyl-C_7	94	90	4	C_7-enes	90	78	12
Trimethyl-C_8	105	99	6	C_8-enes	90	77	13
Triptane	112.8	101.3	11.5				

We hypothesized that the HOG product P/O ratio could be shifted using catalyst design principles that alter the relative hydrogenation and dehydrogenation activity during DME homologation, and consequently, the fuel properties could be manipulated under the same reaction conditions and without additional processing steps that would add capital and operating costs in a biorefinery. This approach is akin to the catalyst design principles that resulted in a shift in the relative aromatic/olefin cycle propagation in methanol-to-olefins chemistry, and to the fuel-property-first approach for biofuels processes [20–22]. In our development of the multi-functional Cu/BEA catalyst, we identified that in addition to the homologation and hydrogen-transfer reactions catalyzed at zeolite Brønsted acid sites, ionic Cu^{1+} species dehydrogenated alkanes and metallic Cu facilitated hydrogenation chemistry (Fig. 1) [12,23]. We further demonstrated that dehydrogenation of light alkanes occurred during DME homologation with co-fed H_2 under mild conditions [13]. Considering the high activation energy that was calculated for dehydrogenation at Cu^{1+}, we postulated that known dehydrogenation active species, specifically those based on ionic Zn [24,25] and Ni [26], may enable increased dehydrogenation activity compared to the Cu/BEA catalyst. Here we report the synthesis, characterization, and DME homologation performance of bimetallic catalysts based on Cu/BEA, with incorporated Zn or Ni. The bimetallic catalysts shifted the P/O ratio and the resulting calculated fuel properties of the C_{5-8} hydrocarbon product mixture. The ability to shift the fuel properties in this manner represents a unique advantage in the catalytic pathway for the conversion of DME to HOG.

2. Experimental

2.1. General

Beta zeolite (BEA) having a SiO_2:Al_2O_3 ratio of 27 (Si:Al = 13.5) was obtained in ammonium form from Tosoh and had a particle/agglomerate size range of 45−125 μm. It was calcined under flowing air at 550 °C to give the proton-form, H-BEA. DME was purchased from Sigma-Aldrich. UHP H_2 and UHP Ar were purchased from General Air and the 1% isobutane/Ar was purchased from Airgas. All gases were used as received. All volumetric flow rates are given at NTP (20 °C, 101.3 kPa) and all pressures are absolute.

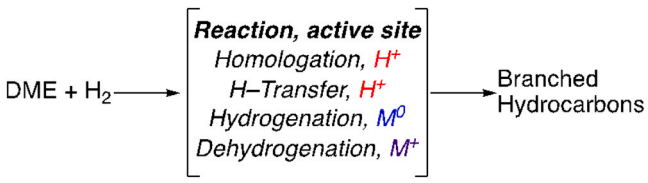

Fig. 1. Schematic of reaction pathways and corresponding active sites for DME homologation with co-fed H_2 over metal-modified BEA zeolite catalysts.

2.2. Catalyst preparation

Mono-metallic ion-exchange catalysts (IE-M/BEA) for isobutane dehydrogenation and ethylene hydrogenation experiments were prepared by aqueous ion-exchange of H-form BEA (0.99 g) with $Cu(NO_3)_2 \bullet 2.5\ H_2O$ (0.061 g), $Ni(NO_3)_2 \bullet 6\ H_2O$ (0.077 g) or $Zn(NO_3)_2 \bullet 6\ H_2O$ (0.077 g) in 40 mL of deionized water. The suspension was stirred for 2–3 h at room temperature, followed by isolation of the material via centrifugation at 7500 rpm for 3 min, and rinsing with 30 mL of deionized water. These materials are termed IE-M/BEA. The benchmark mono-metallic IW-Cu/BEA was prepared as previously described via an incipient wetness impregnation procedure [12], and is referred to throughout as simply Cu/BEA. Bimetallic catalysts were prepared analogously to Cu/BEA, via aqueous incipient-wetness impregnation of IE-M/BEA catalysts with $Cu(NO_3)_2 \bullet 2.5\ H_2O$ (i.e., IW-Cu-IE-M/BEA). Bimetallic catalysts are referred to as Cu-M/BEA (M = Zn or Ni). All catalysts were calcined *ex situ* in a box furnace at 500 °C (2 °C min^{-1} ramp rate) with flowing air for at least 6 h prior to loading into the reactor. Metal contents were determined by inductively coupled plasma optical emission spectroscopy (ICP-OES) at Galbraith Laboratories (Knoxville, TN).

2.3. Characterization

2.3.1. Acid site characterization

The density of Brønsted acid sites (BAS) on each catalyst was quantified by temperature programmed desorption (TPD) of adsorbed isopropylamine (IPA) [27]. Catalyst samples (ca. 200 mg) were reduced under 150 $cm^3\ min^{-1}$ of 95% H_2 / 5% Ar at 300 °C (2 °C min^{-1}) and held for 2 h. After pretreatment, the catalyst was cooled to 100 °C in inert gas (95% N_2 / 5% He). When the bed temperature stabilized at 100 °C for 15 min, 1 mL of IPA was slowly introduced via syringe injection over the course of 10 min. After flushing with inert gas for at least 12 h at 100 °C to remove weakly adsorbed IPA, the temperature was ramped to 500 °C at 10 °C min^{-1}. Desorbed products were analyzed and quantified on a Pfeiffer PrismaPlus mass spectrometer, with propylene used to quantify BAS density. The propylene signal ($m/z = 41$) was calibrated with 5 mL propylene pulses and normalized to the internal standard He ($m/z = 4$) signal.

2.3.2. X-ray absorption spectroscopy (XAS)

Cu, Ni, and Zn K edge X-ray absorption spectra (XAS) were collected on the bending magnet beamline of the Materials Research Collaborative Access Team (MR-CAT) at the Advanced Photon Source, Argonne National Laboratory. Measurements were made in transmission mode from approximately 250 eV below to 600 eV above the absorption edges (step size = 0.3 eV, count time = 0.2 s/step). During each measurement a spectrum of the corresponding metal foil was collected simultaneously, using a third ion-chamber in series, for absolute energy calibration. Catalyst samples were pressed into self-supporting wafers in a stainless-steel holder containing six wells. The holder was sealed in a quartz reactor tube using two Ultra-Torr fittings with Kapton windows and ball valves through which gases could be flowed. The samples were heated to the respective temperatures under a flow of either 20% O_2/He or 3.5% H_2/He, treated for an hour, and then the reactor was purged with He while cooling. Once at room temperature the ball valves were closed, isolating the samples in a static He atmosphere, and spectra were collected. After reduction, the XANES of the IE-Cu/BEA sample was consistent with a mixture of Cu^{1+} and Cu^{2+}. To minimize the chances of the dispersed Cu^{1+} species oxidizing due to small leaks, spectra were collected at high temperature under flowing gases rather than at room temperature and after purging with He. The spectrum of IE-Cu/BEA at 150 °C in 20% O_2/He was essentially identical to that collected at room temperature. However, the spectrum collected at 300 °C in 3.5% H_2/He showed the catalyst contained primarily Cu^{1+} with only a small fraction of Cu^{2+} remaining. Since temperature has minimal effect on the XANES, the spectrum acquired at 300 °C in 3.5% H_2/He was used as a Cu^{1+} reference for linear combination fits of the XANES to estimate the fraction of each oxidation state in the reduced catalysts. Cu foil and the room temperature, post oxidation spectrum were used as Cu^0 and Cu^{2+} references, respectively. Post reduction, the Ni K edge spectrum of IW-Cu-IE-Ni/BEA indicated a small fraction of metallic Ni was present in the sample. As the Ni^{2+} species present in the sample is likely similar to that in IE-Ni/BEA (which contained only oxidized Ni), the post-reduction spectrum of the latter was used as a Ni^{2+} reference for a linear combination fit of the former. The spectrum of Ni foil was used as the Ni^0 reference.

Data processing and analysis were performed using the Demeter software suite [28]. Standard procedures were used for normalization and background subtraction. The distributions of Cu and Ni oxidation states were determined from linear combination fits of the XANES. Coordination parameters were determined from simultaneous least-squares fits in R-space of the magnitude of Fourier transform of the k^1, k^2, and k^3-weighted EXAFS. Theoretical phase shift and backscattering amplitudes were calculated using FEFF6 [29]. Amplitude reduction factors (S_0^2) for Cu (0.86), Ni (0.85), and Zn (0.86) were determined from references with known coordination numbers (Cu foil, Ni foil, Zn acetylacetonate) and these values were fixed in fits of the samples.

2.3.3. Transmission electron microscopy (TEM)

Scanning transmission electron microscopy (STEM) was performed on a JEOL 2200FS STEM/TEM instrument equipped with a CEOS GmbH (Heidelberg, Ger) corrector on the illuminating lenses. The AMAG 5 C mode was used to achieve a probe with a nominal 150 pA current and associated resolution of a nominal 0.07 nm. The presence and distribution of Cu, Ni, Zn in the Cu-M/BEA catalysts were confirmed by utilizing energy dispersive X-ray spectroscopy (EDS) analysis and acquiring spectrum images with a Bruker-AXS silicon-drift detector system (SDD) on the JEOL 2200FS STEM/TEM.

2.4. Isobutane dehydrogenation

Isobutane dehydrogenation activity was evaluated using a packed bed reactor system. For IE-M/BEA catalysts, pre-oxidized catalyst (ca. 360 mg), diluted with inert silicon carbide (ca. 5.4 g), was loaded in the isothermal zone of a 7.9 mm ID stainless steel tubular packed bed reactor while being supported by quartz chips and quartz wool. The catalyst was heated to 300 °C (at 2 °C min^{-1}) in Ar (5 $cm^3\ min^{-1}$) and dried for at least 2 h. Subsequently, the catalyst was exposed to 1% isobutane/Ar (25 $cm^3\ min^{-1}$) at 300 °C and 200 kPa for > 8 h while analytical samples were collected. The WHSV of isobutane was 0.10 $g_{isobutane}\ g_{cat}^{-1}\ h^{-1}$, and the isobutane partial pressure was 2 kPa.

A prior report from our group has demonstrated that Cu^{2+} species are rapidly converted to Cu^{1+} during isobutane conversion, and that reductive pre-treatment of IE-Cu/BEA does not affect its H_2 STY for isobutane dehydrogenation [23]. The reaction temperature of 300 °C was chosen to obtain meaningful activity given existing reactor system and analytical constraints. The equilibrium conversion for isobutane to form isobutene under the conditions utilized here is 8.3%. Isobutane conversion above equilibrium conversion was observed in some cases, and this is attributed to secondary reactions of the product, isobutene, at Brønsted acid sites that initiate/propagate the hydrocarbon chain-growth cycle, as described below.

Reactor inlet lines were heated to 150 °C to preheat influent gases and outlet lines were heated to 200 °C to prevent condensation of hydrocarbons. The gas composition was quantified using an Agilent 7890 GC equipped with a flame ionization detector for analysis of oxygenates and hydrocarbons and two thermal conductivity detectors for analysis of permanent gases and water. GC response factors for reactants and products were calibrated using traceable gravimetric gas standards. The gravimetric rate of H_2 formation (r_{H2}, in $mol_{H2}\ g_{cat}^{-1}\ h^{-1}$) was calculated according to Eq. 3:

$$r_{H2} = \frac{\dot{n}_{H2}}{m_{cat}} \quad (3)$$

where $\dot{n}_{H2}$ is the effluent molar rate of H_2 (mol_{H2} h^{-1}) and m_{cat} is the total catalyst mass (g). The H_2 site time yield (STY, in mol_{H2} mol_M^{-1} s^{-1}) was calculated according to Eq. 4:

$$STY_{H2} = \frac{r_{H2}}{m_M} \quad (4)$$

where r_{H2} is the gravimetric formation rate of H_2 converted to μmol g_{cat}^{-1} s^{-1} and m_M is the metal loading of M (i.e., Zn, Ni or Cu) in μmol_M g_{cat}^{-1}.

For Cu/BEA and bimetallic catalysts, isobutane dehydrogenation activity was evaluated using an identical system and similar procedure as those used for mono-metallic IE-M/BEA catalysts. Pre-oxidized catalyst (ca. 360 mg), diluted with inert silicon carbide (ca. 5.4 g), was loaded in the isothermal zone of a 7.9 mm ID stainless steel tubular packed bed reactor while being supported by quartz chips and quartz wool. The catalyst was heated to 300 °C (at 2 °C min^{-1}) in H_2 (25 cm^3 min^{-1}) and held for 2 h. Following reduction, the catalyst was kept at 300 °C in Ar (5 cm^3 min^{-1}) until isobutane flow began. Subsequently, the catalyst was exposed to 1% isobutane/Ar (25 cm^3 min^{-1}) at 300 °C and 200 kPa for > 8 h while analytical samples were collected. The WHSV of isobutane was 0.10 $g_{isobutane}$ g_{cat}^{-1} h^{-1}, and the isobutane partial pressure was 2 kPa.

Due to the possibility of activating *in situ* generated H_2 over the Cu/BEA and bimetallic catalysts as a result of their metallic site fraction, the activity of these materials in isobutane probe reactions is presented with two metrics. The gravimetric rate of H_2 formation (Eq. 3), and the rate of hydrocarbon formation, expressed as the catalyst mass-normalized carbon molar rate, r_C, calculated according to Eq. 5:

$$r_C = \frac{\sum \dot{n}_i * \nu_i}{m_{cat}} \quad (5)$$

where $\sum \dot{n}_i$ is the effluent molar rate of product i (mol_i s^{-1}), summed over all observed hydrocarbon products, ν_i is the stoichiometric coefficient for product i (mol_C mol_i^{-1}) and m_{cat} is the total catalyst mass loading (g).

2.5. Ethylene hydrogenation

Ethylene hydrogenation activity was evaluated using a fixed bed reactor system with co-fed H_2. Pre-oxidized catalyst (ca. 360 mg), diluted with inert silicon carbide (ca. 5.4 g), was loaded in a ca. 5 mm ID quartz tube reactor, supported by quartz wool with a thermocouple to monitor and control reactor temperature positioned at the top of the catalyst bed. The catalyst was reduced in flowing H_2 (25 cm^3 min^{-1}) for at least 2 h at 300 °C (at 2 °C min^{-1}) before cooling to 100 °C. Subsequently, the catalyst was exposed to 2.5% ethylene/He (25 cm^3 min^{-1}) at 100 °C and 200 kPa for > 7 h while analytical samples were collected. The WHSV of ethylene was 7.0 $g_{ethylene}$ g_{cat}^{-1} h^{-1}, with $p_{ethylene} = 2$ kPa, and $p_{H2} = 20$ kPa, with the remainder p_{He}. The reaction temperature of 100 °C was selected to obtain sub-complete conversion over all materials and to limit formation of byproducts.

Reactor system lines were heated to > 100 °C to preheat influent gases and prevent condensation of effluent products. The gas composition was quantified using an Agilent 490 Micro GC equipped with four thermal conductivity detectors for analysis of oxygenates, hydrocarbons, permanent gases and water. GC response factors for reactants and products were calibrated using traceable gravimetric gas standards.

The gravimetric rate of ethane formation, r_{ethane}, was calculated according to Eq. 6:

$$r_{ethane} = \frac{\dot{n}_{ethane,out}}{m_{cat}} \quad (6)$$

where $\dot{n}_{ethane,out}$ is the flow rate of ethane out of the reactor in mol s^{-1}, and m_{cat} is the total catalyst mass loading (g).

2.6. Dimethyl ether homologation

Pre-oxidized catalyst powders were pressed (22 kN), crushed in a porcelain mortar and pestle, and sieved to 212–300 μm (50–70 mesh). The catalyst (0.325 g) was diluted with ca. 5.3–5.8 g low surface-area, inert silicon carbide to achieve a constant catalyst bed volume, and to minimize channeling, axial dispersion, and temperature gradients in the bed. Catalysts were loaded into a 7.9 mm ID stainless-steel tubular reactor and positioned within the isothermal zone using quartz chips and quartz wool. A four-point thermocouple positioned within the catalyst bed was used to monitor reaction temperature. The reaction temperature during an experiment was maintained within ± 0.5 °C of the nominal setpoint. The catalyst was reduced in flowing H_2 at 25 cm^3 min^{-1} for at least 3 h at 300 °C before cooling to 200 °C. Immediately following the reduction, the catalyst was exposed to the reaction mixture, and reactor outlet gas sampling began. In all experiments, the DME WHSV was ca. 2.2 g_{DME} g_{cat}^{-1} h^{-1} (referred to as h^{-1}). The reaction gas flow rates were 6.1, 6.1, 1.0 cm^3 min^{-1} for DME, H_2, Ar, respectively, where Ar was used as an internal standard. Time-on-stream (TOS) is defined as the cumulative time elapsed from the start of DME flow. The gas composition at the inlet of the reactor was quantified at the conclusion of each experiment.

Reactor inlet and outlet gases were sampled through heated (170 °C) lines with an Agilent 7890 GC instrument equipped with a flame ionization detector for analysis of oxygenates and hydrocarbons and two thermal conductivity detectors for analysis of permanent gases. GC responses for reactants and products were calibrated using traceable gravimetric gas standards. Carbon balances in these reactions were within ± 7%. Catalyst performance was evaluated from inlet flow and GC measurements using Ar as an internal standard. Turnover number (TON) values are reported as the cumulative mol of carbon in hydrocarbon products per mol of Brønsted acid sites in the reactor at each time point [30], as represented in Eq. 7:

$$TON(t) = \frac{1}{N_{H+}} \int_0^t dt' n_C(t') \quad (7)$$

where t is TOS in h, N_{H+} is the moles of Brønsted acid sites, and $n_c(t')$ is the total carbon incorporated (mol carbon h^{-1}) in all products except methanol, carbon monoxide and carbon dioxide at time t'. The conversion, X (in carbon %), was calculated according to Eq. 8 based on the hydrocarbon product formation rate and the inlet DME molar flow rate:

$$X = \frac{\dot{n}_{C,HC-products}}{\dot{n}_{C,DME,in}} * 100\% \quad (8)$$

where $\dot{n}_{C,DME,in}$ and $\dot{n}_{C,HC\text{-}products}$ represent the molar flow rates of carbon (mol_C s^{-1}) in DME and hydrocarbon products, respectively. The term, $\dot{n}_{C,HC\text{-}products}$, excludes methanol and trace CO. The methanol-free product carbon selectivity, $_{Si}$ (in carbon %), was calculated via Eq. 9:

$$S_i = \frac{\dot{n}_{C,i}}{\sum \dot{n}_{C,i}} * 100\% \quad (9)$$

where $\dot{n}_{C,i}$ represents the effluent molar flow rate of carbon in individual products (mol_C s^{-1}), excluding methanol. DME homologation data for Cu/BEA is reported as the mean of at least 3 independent experiments. The standard error of the mean (SEM) was included as error bars for Cu/BEA data calculated as the standard deviation divided by the square-root of the number of data points used in the reported mean. Experiments with Cu-Ni/BEA and Cu-Zn/BEA are reported as the mean of 2 independent experiments, therefore SEM was not calculated. Error bars for Cu-Ni/BEA and Cu-Zn/BEA data represent the range of the two data points used to calculate the mean.

2.7. Octane number calculation

The predicted RON and MON for gasoline-range hydrocarbon mixtures were calculated using Eq. 10, as reported by Ghosh et al. [10]:

$$ON_{mix} = \frac{\sum_{PONA} v_i \beta_i ON_i + I_p \sum_p v_i \beta_i ON_i}{\sum_{PONA} v_i \beta_i + I_p \left(\sum_p v_i \beta_i - \sum_p v_i \right)} \quad (10)$$

where ON_{mix} can be RON_{mix} or MON_{mix}, and $\sum_{PONA}$ and $\sum_P$ are summations over paraffins, olefins, naphthenes, aromatics (i.e., PONA) and paraffins (i.e., P), respectively. The v_i, β_i, ON_i, and I_P represent the volume fraction (here, estimated as mol fraction in the gas-phase GC analysis) of species *i* in the sample, molecular lumped blend parameter of species *i*, pure component octane number (RON or MON) of species *i*, and the interaction term describing the nonlinear interaction between paraffins and naphthenes or olefins, respectively. The β_i, ON_i values were used as reported in Ghosh et al. The sensitivity (S) was calculated as the difference between the RON and the MON values.

3. Results and discussion

3.1. Catalyst design, synthesis, and characterization

3.1.1. Bimetallic catalyst design informed from mono-metallic M/BEA catalysts

The design of bimetallic catalysts was motivated by a preliminary assessment of dehydrogenation activity for mono-metallic Cu, Ni, and Zn sites in BEA zeolite. We previously demonstrated that the parent H-BEA is inactive for isobutane dehydrogenation, but ionic Cu^{1+}-BEA sites are active for this chemistry [23]. Ionic Zn and Ni species are known dehydrogenation active sites for light (C_{2-4}) alkanes, where the recent focus has been on the conversion of propane to propene [24–26]. Catalysts based on Ag, In, and Ga have also been investigated, but we chose to focus our initial assessment on earth-abundant and relatively inexpensive Zn and Ni species [32–35]. Aqueous ion-exchange (IE) of the respective metal nitrate solution provided comparable molar metal loadings in IE-M/BEA materials, ranging from 135 to 153 μmol g_{cat}^{-1}. X-ray absorption spectroscopy (XAS) confirmed the presence of ionic metal sites following reduction at 300 °C, consistent with exchange at Brønsted acid sites (BAS), without any metallic Cu, Ni, or Zn observed (Tables S1 and S2, Fig. S1-S8). Isobutane dehydrogenation serves as a relevant probe reaction due to the high selectivity to isobutane (35–40%) and low selectivity to C_{2-3} olefins (< 3%) over BEA catalysts in DME homologation [5,12,23]. The isobutane dehydrogenation activity of each catalyst was evaluated at 300 °C and 200 kPa. These conditions were chosen to provide measurable H_2 production rates (Fig. 2A), which were monitored as a quantitative indicator of dehydrogenation activity and normalized to the molar metal loading to give site-time yield (STY) values (Fig. 2B) [23]. After the induction period of ca. 8 h time-on-stream (TOS), the H_2 formation rates for IE-Ni/BEA (52.7 μmol g_{cat}^{-1} h^{-1}) and IE-Zn/BEA (22.5 μmol g_{cat}^{-1} h^{-1}) were greater than the rate from IE-Cu/BEA (8.62 μmol g_{cat}^{-1} h^{-1}). Accordingly, the STY values indicate greater dehydrogenation activity for IE-Ni/BEA (10.6×10^{-5} mol_{H2} mol_M^{-1} s^{-1}) and IE-Zn/BEA (4.6×10^{-5} mol_{H2} mol_M^{-1} s^{-1}) compared to IE-Cu/BEA (1.5×10^{-5} mol_{H2} mol_M^{-1} s^{-1}). These results support our hypothesis that ionic Ni and Zn active sites have higher activity than ionic Cu sites for alkane dehydrogenation under these relatively mild conditions.

3.1.2. Synthesis of bimetallic catalysts and acid site characterization

In addition to alkane dehydrogenation activity, the activation of co-fed H_2 by metallic Cu species during DME homologation is an essential function of the Cu/BEA catalyst that leads to enhanced performance [12]. To this end, bimetallic catalysts were synthesized with a two-step method, where the Ni or Zn was first incorporated at a low metal loading (< 1 wt%) using the ion-exchange method described above. After oxidation of the IE-M/BEA material at 500 °C, Cu was deposited via incipient wetness impregnation (IW) at a higher metal loading (4–5 wt %) to promote the formation of metallic Cu after oxidation at 500 °C and subsequent reduction at 300 °C. This method yielded bimetallic materials with metal weight loadings reported in Table 2. A Cu/BEA catalyst was prepared using a one-step IW procedure as a benchmark comparison for the bimetallic materials. BAS densities were determined using isopropylamine temperature-programmed desorption (IPA-TPD) (Table 2, Fig. S9). The observed BAS densities are consistent with ion-exchange of BAS with ionic metal sites, as observed for Cu/BEA compared to H-BEA and similar metal-modified zeolites [12,21,36].

3.1.3. X-ray absorption spectroscopy

The oxidation states for Cu, Ni, and Zn species were determined after oxidation and reduction using XAS (Tables S1 and S2, Fig. S1-S8), which enabled quantification of the ionic and metallic content of the catalysts (Table 3). The ionic content represents the expected dehydrogenation site density. The metallic content represents the total amount of metallic species in the metal particles (i.e., not just the surface metal sites), and while not a direct measure of the hydrogenation site density, provides useful information for comparison of the structural differences between the catalysts. The Cu species in Cu-Ni/BEA were a mix of metallic (80%)

Table 2
Metal loadings and Brønsted acid site (BAS) densities for the bimetallic catalysts and the benchmark Cu/BEA catalyst. BAS densities were determined using IPA-TPD.

Catalyst	Metal loadings Cu; M (wt%)	BAS density (μmol g^{-1})
Cu/BEA	4.3	925
Cu-Ni/BEA	4.6; 0.71	830
Cu-Zn/BEA	4.3; 0.77	785

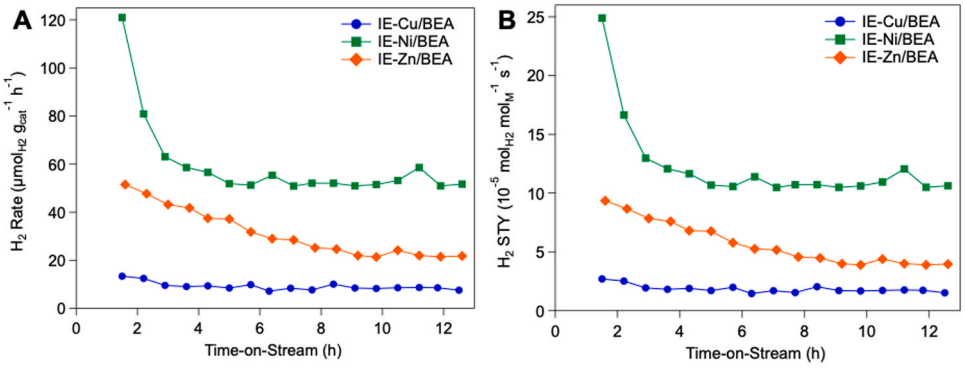

Fig. 2. (A) H_2 formation rate and (B) STY of H_2 over IE-M/BEA catalysts during isobutane dehydrogenation as a function of TOS. Reaction performed at 300 °C, 200 kPa, isobutane WHSV of 0.10 $g_{isobutane}$ g_{cat}^{-1} h^{-1}, and $p_{isobutane}$ = 2 kPa.

Table 3
Ionic and metallic site densities for the bimetallic catalysts compared to the benchmark Cu/BEA catalyst. Content of each species or group of species was calculated from XAS oxidation states and ICP-OES metal loading (Table S1).

Catalyst	Total ionic content (μmol g^{-1})	Total metallic content (μmol g^{-1})	Ionic Cu content (μmol g^{-1})	Ionic Ni or Zn content (μmol g^{-1})
Cu/BEA	120	555	120	–
Cu-Ni/BEA	235	600	145	90
Cu-Zn/BEA	350	450	230	120

and ionic (20%) Cu, similar to that observed for Cu/BEA (82% metallic, 18% ionic). For the Ni species, 24% of Ni was in the reduced metallic form, and 76% remained as Ni^{2+}. The metallic Ni content equates to 0.17 wt% (30 μmol g^{-1}), which when combined with the metallic Cu content (3.7 wt%, 570 μmol g^{-1}), gives a total of 3.9 wt% (600 μmol g^{-1}) metallic species. The combined ionic Ni and Cu content equates to 1.5 wt% (235 μmol g^{-1}). Thus, Cu-Ni/BEA contains a comparable amount of total metallic species to Cu/BEA (4.3 wt%, 555 μmol g^{-1}) and nearly double the ionic metal species versus Cu/BEA (120 μmol g^{-1}). The Cu species in Cu-Zn/BEA were a mix of metallic (66%) and ionic (34%) species, again similar to that observed for Cu/BEA. The Zn species remained Zn^{2+} after reduction, consistent with the IE-Zn/BEA above and with previous investigations where isolated Zn^{2+} species were observed after reductive pre-treatments [25]. Cu-Zn/BEA possesses a lower metallic species content than Cu/BEA (450 vs 555 μmol g^{-1}), but a 3-fold increase in ionic metal loading (350 versus 120 μmol g^{-1}).

3.1.4. Transmission electron microscopy and elemental mapping

Scanning transmission electron microscopy (STEM) imaging with energy dispersive spectroscopy (EDS) was employed to investigate the spatial distribution of the metal species. The catalysts were analyzed after oxidation at 500 °C and reduction at 300 °C to mimic the activation procedure used in subsequent DME homologation reactions. After reduction, the catalysts were passivated at room temperature with 1% O_2/N_2 prior to STEM analysis. Although the catalysts were not characterized in their fully reduced form, any metallic interfaces or alloys that formed during reduction were assumed to remain co-located as oxides after mild oxidative passivation. The bright-field (BF)-STEM image and EDS elemental maps for the Cu-Ni/BEA catalyst displays both Cu and Ni signals in the larger metal particles, suggesting co-localization of Cu and Ni within the same particle (Fig. 3A). Nanoparticles of metallic Cu without Ni incorporation as well as nanoparticles of metallic Ni without Cu were also observed (Fig. S10). In contrast, the Zn species were more uniformly distributed on the BEA zeolite without preferential co-location with Cu particles (Fig. 3B). These results support the XAS analysis, indicating spatially resolved metallic Cu and ionic Zn species in the Cu-Zn/BEA catalyst, and a fraction of reduced metallic Ni in the Cu-Ni/BEA catalyst. The combination of characterization techniques reveals that the Cu-Ni/BEA catalyst consists of isolated Ni^{2+} sites, isolated Cu^{1+} sites, metallic Ni, metallic Cu, and possibly alloyed CuNi metal. The Cu-Zn/BEA catalyst consists of ionic Zn^{2+} and Cu^{1+} sites, and metallic Cu.

3.2. Hydrogenation and dehydrogenation probe reactions

The bimetallic catalysts and the benchmark Cu/BEA were tested in two probe molecule reactions, ethylene hydrogenation and isobutane dehydrogenation, to assess the activity of metallic sites and ionic sites, respectively, as outlined in Fig. 1. Ethylene hydrogenation was chosen because neither ethylene nor ethane participates in the subsequent olefin-cycle hydrocarbon pool chemistry, according to the reported mechanism [37]. Ethane was the only observed product in these reactions (i.e., 100% selectivity), therefore the ethane production rate was taken as a quantitative indicator of hydrogenation activity (Fig. 4A). Comparing at ca. 2.5 h TOS, the Cu-Ni/BEA catalyst was ca. 250-fold more active than Cu/BEA (47.9 and 0.17 μmol g_{cat}^{-1} s^{-1}, respectively). The marked increase in hydrogenation activity exhibited by Cu-Ni/BEA relative to Cu/BEA and Cu-Zn/BEA is attributed to the metallic Ni species, which are well-known hydrogenation catalysts. It is worth noting that the hydrogenation activity of Cu-Zn/BEA is approximately the same order of magnitude as Cu/BEA, and the observed increase in activity may be attributed to different Cu particle sizes, which were not attempted to be controlled in these materials.

Isobutane dehydrogenation was performed under reaction

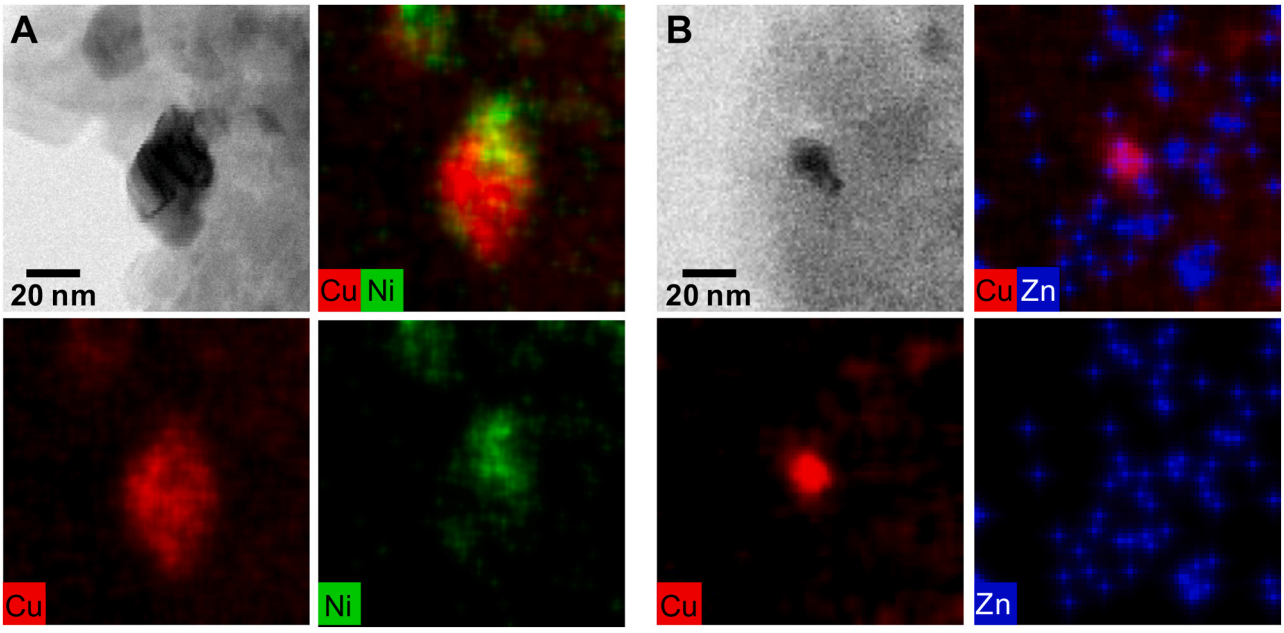

Fig. 3. BF-STEM images with EDS elemental maps for (A) Cu-Ni/BEA and (B) Cu-Zn/BEA after *ex situ* oxidation in air at 500 °C, reduction in H_2 at 300 °C, and passivation in 1% O_2/N_2 at room temperature.

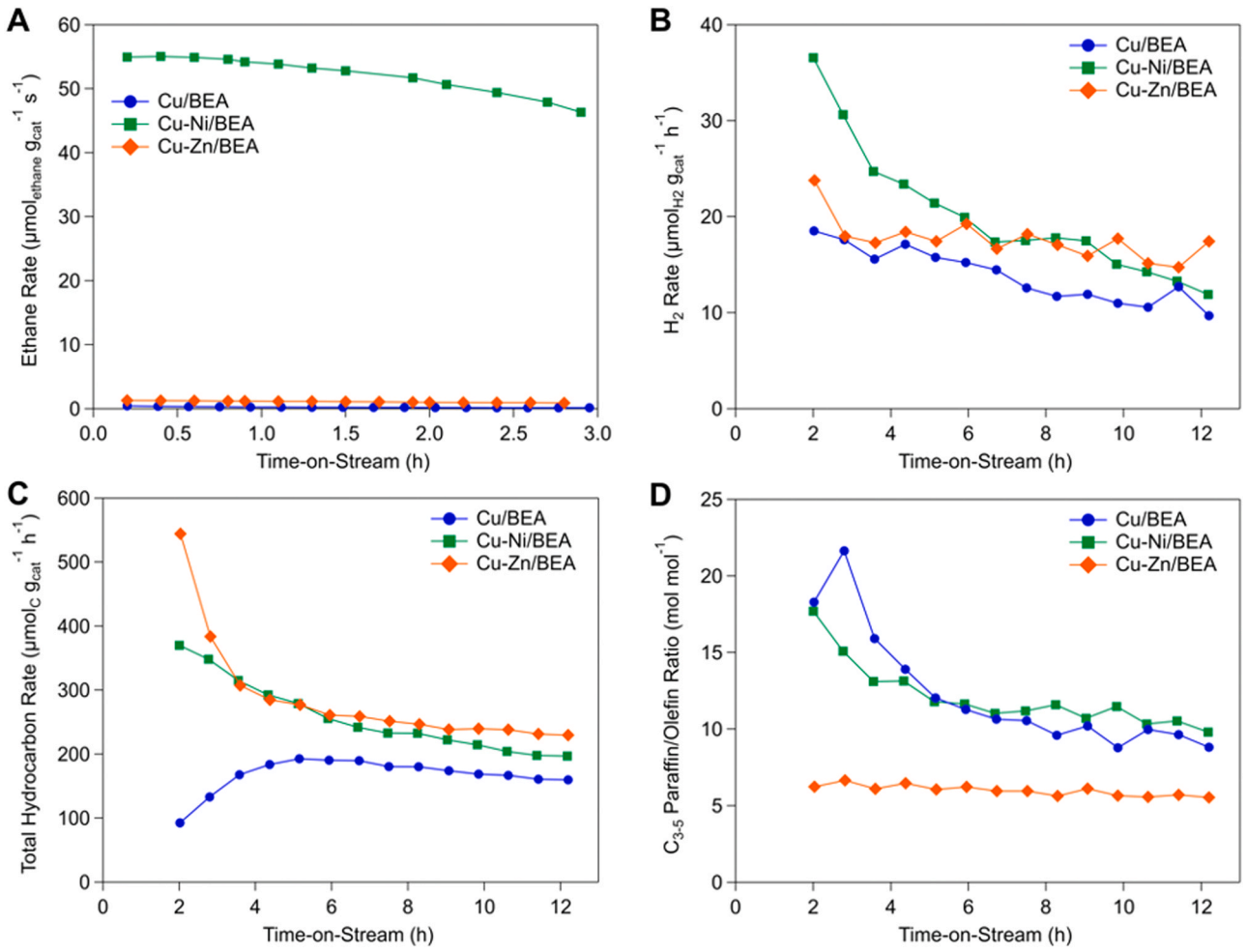

Fig. 4. (A) Plot of ethane rate from ethylene hydrogenation reactions, (B) rate of hydrogen formation from isobutane dehydrogenation reactions, (C) rate of hydrocarbon formation from isobutane dehydrogenation reactions, and (D) paraffin/olefin product ratio of C_{3-5} products from isobutane dehydrogenation reactions. Reaction conditions for (a) were 100 °C, 200 kPa, ethylene WHSV of ca. 7.0 h^{-1}; $p_{ethylene}$ and p_{H2} were 2 and 20 kPa, respectively, remainder p_{He}, and for (b-d) were 300 °C, 200 kPa, isobutane WHSV of 0.10 $g_{isobutane}$ g_{cat}^{-1} h^{-1}, and $p_{isobutane}$ = 2 kPa. Reactant conversions in (A) were 83–98% for Cu-Ni/BEA, 1.6 – 2.3% for Cu-Zn/BEA, and 0.2 – 1.0% for Cu/BEA. Reactant conversion values in (B-D) were between 2.1% and 4.9% after 6 h TOS for all catalysts.

conditions identical to those used with the mono-metallic IE-M/BEA catalysts described above. As reported before, isobutane activation is facilitated by dehydrogenation at ionic sites but not metallic Cu sites [23], and once the olefin is formed, it may react with Brønsted acid sites to initiate the hydrocarbon chain-growth cycle [6,7]. The metallic sites in Cu/BEA, Cu-Ni/BEA and Cu-Zn/BEA can activate and incorporate the *in situ*-generated H_2 into secondary reactions of isobutene [12], and therefore, the STY based on H_2 production per total ionic site content in the Cu-Ni/BEA, Cu-Zn/BEA and Cu/BEA catalysts does not provide a direct metric for comparison. Rather, both the H_2 production rate and the total hydrocarbon formation rate were used to compare dehydrogenation activity. After 8 h TOS, greater H_2 formation rates were observed for Cu-Ni/BEA and Cu-Zn/BEA (15.0 ± 2.3, 16.3 ± 1.2 μmol_C g_{cat}^{-1} h^{-1}, respectively) compared to Cu/BEA (11.3 ± 1.1 μmol_{H2} g_{cat}^{-1} h^{-1}), representing relative increases of 33% and 44% versus Cu/BEA (Fig. 4B). Similar increases were observed in the hydrocarbon formation rate for Cu-Ni/BEA and Cu-Zn/BEA (212 ± 14, 237 ± 6 μmol_C g_{cat}^{-1} h^{-1}, respectively) compared to Cu/BEA (168 ± 8 μmol_C g_{cat}^{-1} h^{-1}), representing relative increases of 26% and 41% versus Cu/BEA (Fig. 4C). As observed previously, greater than 98% selectivity to C_{3-5} hydrocarbons was observed over all three catalysts [23], and a comparison of the P/O ratio of these products provided the first indication of a shift in the relative hydrogenation and dehydrogenation activity based on catalyst composition. Compared after 8 h TOS, the P/O ratios for Cu/BEA and Cu-Ni/BEA were similar (9.5 ± 0.6 and 10.7 ± 0.7 mol mol^{-1}, respectively), but a substantial reduction to 5.7 ± 0.2 mol mol^{-1} was observed for Cu-Zn/BEA (Fig. 4D). These isobutane probe reaction data indicate that dehydrogenation activity was enhanced for both bimetallic catalysts, and that the Cu-Zn/BEA catalyst promoted olefin formation versus Cu/BEA and Cu-Ni/BEA under these conditions, providing the opportunity to explore the relative hydrogenation and dehydrogenation activity in the more complex DME homologation chemistry.

3.3. DME homologation

Catalysts were tested in the DME homologation reaction with co-fed H_2 at 200 °C and 103 kPa. DME homologation over mono-metallic IE-Cu/BEA, IE-Zn/BEA, and IE-Ni/BEA catalysts is not reported here due to low activity in preliminary experiments compared to Cu/BEA. Conversion values of less than 10% were targeted to compare catalyst selectivities at near-differential conversion conditions, and all three catalysts met this criterion after the initial induction period (Fig. 5A). The Cu-Ni/BEA catalyst exhibited a longer induction period than the other catalysts but achieved a comparable steady-state activity to that of Cu/BEA after about 10 h TOS. The Cu-Zn/BEA was slightly less active than the other catalysts, exhibiting a conversion of ca. 3.8% at 10 h TOS versus ca. 6.5% at 10 h for Cu/BEA and Cu-Ni/BEA. The turnover number (TON) in

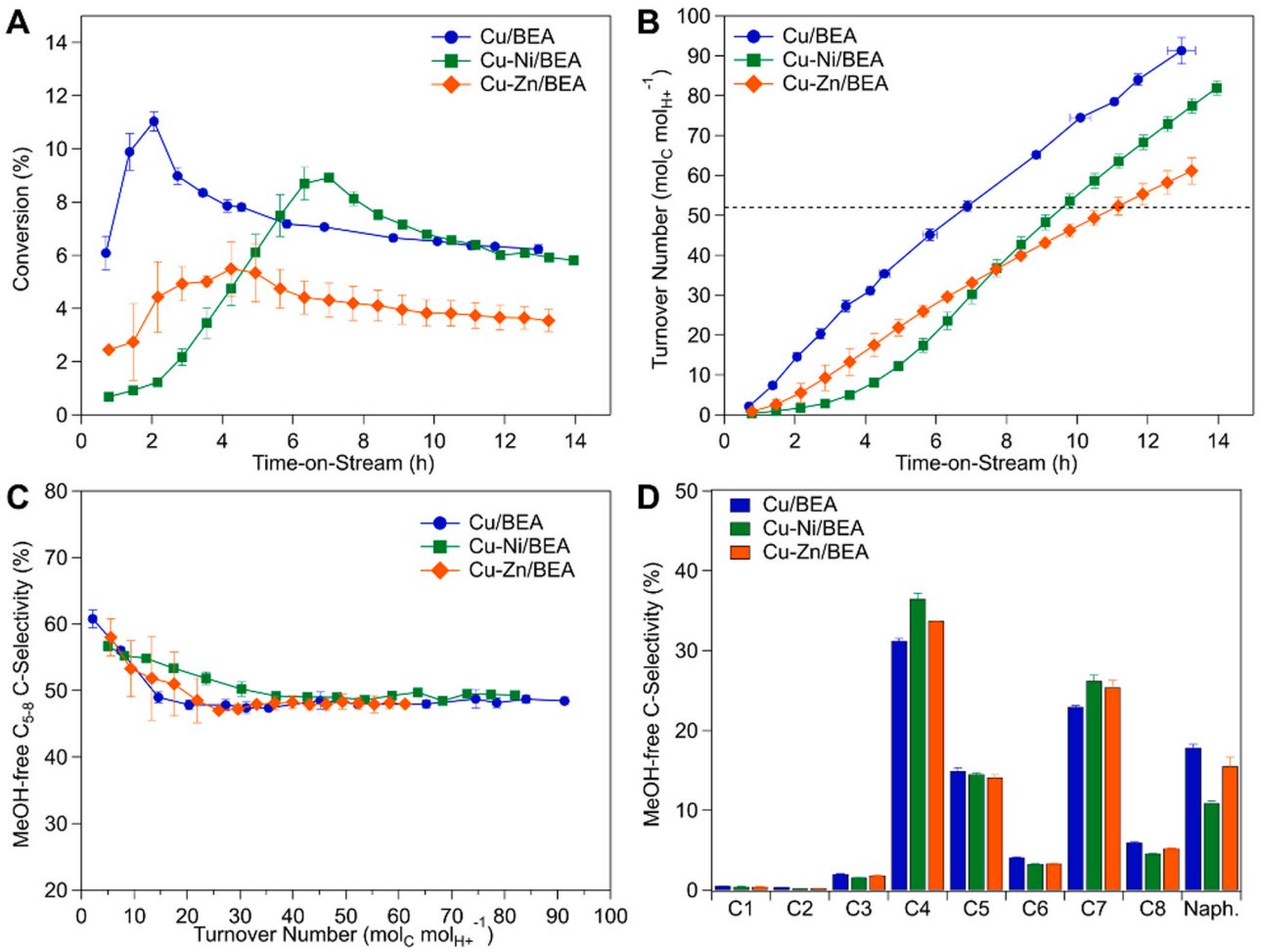

Fig. 5. Plots from DME homologation over Cu/BEA, Cu-Zn/BEA and Cu-Ni/BEA for (A) conversion and (B) TON versus TOS with TON = 52 indicated with a horizontal dashed line. Methanol-free carbon-selectivity for (C) total high-octane gasoline range C_{5-8} hydrocarbons versus TON, and (D) hydrocarbon distribution by carbon number taken at TON = 52 ± 2 mol$_C$ mol$_{H+}^{-1}$. Reaction conditions were 200 °C, 103 kPa, DME WHSV of 2.2 h^{-1}, p_{DME} and p_{H2} each 47 kPa, remainder p_{Ar}. Data are presented as mean ± SEM for Cu/BEA and mean ± range for Cu-Ni/BEA and Cu-Zn/BEA.

this Brønsted-acid-catalyzed homologation reaction is a metric that enables a coherent comparison of the inherently transient chemistry of zeolite catalysts that operate through the hydrocarbon pool, since TON accounts for catalyst loading, acid site density, DME flow rate, and hydrocarbon product yield (Fig. 5B, Fig. S11) [30,38]. A common TON value of 52 ± 2 mol$_C$ mol$_{H+}^{-1}$ was reached for each catalyst, providing a point of comparison for the selectivity values of interest to the P/O ratio.

The methanol-free product carbon-selectivity for the C_{5-8} range products stabilized at ca. 50% for each catalyst after 25–35 turnovers (Fig. 5C), corresponding to 4–7 h TOS (Fig. S12). Comparable methanol-free product carbon-selectivity at a TON of 52 mol$_C$ mol$_{H+}^{-1}$ was observed for the three catalysts, and was consistent with the high selectivity for C_4 and C_7 products that is characteristic for DME homologation over BEA and Cu/BEA (Fig. 5D and Table S3) [5,7,8,12,13]. Previous investigations reported product carbon-selectivity up to C_8 with a focus on the high-octane C_7 product, triptane [5–8]. Here, we included higher carbon-number products in our analysis, and observed the production of naphthenes (i.e., methylated cyclohexanes) from all three catalysts. These cyclic products can be attributed to cyclization reactions of dienes with mono-olefins followed by hydrogenation (e.g., Diels-Alder reactions), intramolecular cyclizations of long-chain trienes followed by hydrogenation, and/or hydrogenation of aromatic intermediates such as hexamethylbenzene, which is the only aromatic product observed in this chemistry over BEA catalysts. Of the observed 11–18% of naphthene products, more than 95% of these are C_{8+} cyclic products for all catalysts, and thus, they do not contribute to the C_{5-8} hydrocarbon HOG product following a conceptual distillation [9], as discussed below. These naphthene products may have been observed and grouped with the C_{8+} product in previous reports, but not discussed in great detail due to the uniquely high selectivity for triptane and the mechanistic aspects that were the focus of those reports [5,6]. Despite similar overall product carbon number distributions, changes in selectivity to specific products are worth noting for the bimetallic catalysts versus the benchmark Cu/BEA (Table S3). A greater *n*-butane selectivity (2.9 versus 0.2%) and reduced naphthene selectivity (11.3 versus 17.8%) was observed for Cu-Ni/BEA compared to Cu/BEA, consistent with increased hydrogenation activity that would promote hydrogenation of C_4 olefins and decreased cyclization chemistry due to hydrogenation of intermediate dienes (e.g., reaction of butenes and butadiene to *n*-butane). Greater isobutene selectivity (7.5 versus 4.1%) was observed for Cu-Zn/BEA compared to Cu/BEA, consistent with increased dehydrogenation activity (e.g., reaction of isobutane to isobutene) (*vide infra*). Overall, the consistent C_{5-8} selectivities exhibited by each catalyst at greater TONs suggest that the fundamental zeolite hydrocarbon pool chemistry (i.e., homologation in Fig. 1) was largely unchanged over these bimetallic catalysts, similar to that observed upon the addition of Cu to BEA zeolite [12,13]. Furthermore, there were no clear trends in C_{5-8} selectivities or P/O ratios with conversion (Fig. S13). Thus, the HOG product P/O ratio was explored in the context of the relative metal-catalyzed hydrogenation and ionic-catalyzed dehydrogenation

activity of the catalysts.

3.4. Paraffin-to-olefin product ratio and calculated fuel properties

The P/O ratio (mol mol^{-1}) stabilized after the initial induction period of 25–35 turnovers, giving 19, 9.4, and 6.6 mol mol^{-1} at TON of 52 mol_C $mol_{H+}{}^{-1}$ for Cu-Ni/BEA, Cu/BEA, and Cu-Zn/BEA, respectively (Fig. 6). The increased paraffin content over Cu-Ni/BEA versus Cu/BEA is attributed to the markedly greater hydrogenation activity of metallic Ni species, as described above for the ethylene hydrogenation probe reaction. Despite the comparable dehydrogenation activity exhibited by Cu-Ni/BEA and Cu/BEA in the isobutane dehydrogenation probe reaction, the metal-based hydrogenation activity has a greater effect on the resulting product slate in DME homologation with co-fed H_2 under these conditions. The decreased P/O ratio exhibited by Cu-Zn/BEA is attributed to enhanced relative dehydrogenation activity due to ionic Zn^{2+} sites, similar to the shift in P/O ratio observed in the isobutane dehydrogenation probe reaction. The ethylene hydrogenation rate for Cu-Zn/BEA was slightly greater than that for Cu/BEA, suggesting that the reduced P/O ratio is not due to a loss of hydrogenation activity for Cu-Zn/BEA versus Cu/BEA. It is unclear if the dehydrogenation turnover frequency for Zn^{2+} sites is greater than Cu^{1+} sites due to the secondary reactions of alkenes in both the isobutane dehydrogenation probe reaction and DME homologation. Thus, we propose that the decrease in the P/O ratio in the C_{5-8} products is due to the increase in total ionic metal content present in the Cu-Zn/BEA versus Cu/BEA (350 versus 120 μmol g^{-1}, respectively). Further experiments are necessary to explore how Zn^{2+} sites may affect H-transfer in the complex dual-cycle mechanism and to fully understand the role of Zn^{2+} sites in reducing the P/O ratio. Similarly, experiments with long times on stream would be necessary to probe changes to the metal speciation and any effects on the P/O ratio after extended reaction times. Nevertheless, compared to the benchmark Cu/BEA catalyst, Cu-Ni/BEA and Cu-Zn/BEA demonstrate shifts in net hydrogenation and dehydrogenation of the C_{5-8} product mixture, resulting in markedly different P/O ratios (i.e., 19 versus 6.6 mol mol^{-1}, respectively). This was accomplished using catalyst design principles, rather than changes to the reaction conditions or addition of unit operations.

Liquid products could not be collected at the volumes necessary for physical octane number measurements; however, the RON, MON, and corresponding S value were calculated using the method reported by Ghosh et al. [10] These calculations were performed on the C_{5-8} product mixture at the TON of 52 mol_C $mol_{H+}{}^{-1}$. This selected C_{5-8} product mixture represents the HOG product from a conceptual distillation to separate light species (e.g., unreacted DME and H_2, C_{1-4} products) and any residual heavy species (e.g., C_{8+} naphthenes) from the desired C_{5-8} products [9,31]. The values are presented in Fig. 7 and compared with two gasoline benchmarks – regular U.S. gasoline (Reg-E10) and premium U.S. gasoline (Prem-E10) both containing 10 vol% ethanol [39]. A representative refinery alkylate stream (98 RON and 93.5 MON), which is used as a blendstock to increase octane in gasoline, is also included for comparison to the HOG products [40]. The products from each catalyst have high RON values of 98–99, comparable to alkylate and exceeding that of premium fuel (97), thus highlighting the desirable high-octane nature of this fuel product compared to a traditional methanol-to-gasoline (MTG) product that resembles regular gasoline (91 RON) [41]. As expected, the MON values for the HOG products decreased with decreasing P/O ratio (i.e., increasing olefin content), from 88 for Cu-Ni/BEA to 87 for Cu/BEA and 85 for Cu-Zn/BEA. The corresponding S values increased from 10 to 12 and 14 for Cu-Ni/BEA, Cu/BEA, and Cu-Zn/BEA, respectively, greatly exceeding that of alkylate (4.5). For Cu-Ni/BEA, the product has the same S as premium fuel, but with higher independent RON and MON values. For Cu-Zn/BEA, the product has a notably greater S of 14, and maintains a high RON value (99).

The importance of both high RON and high S is further contextualized using the recently developed gasoline efficiency merit function [19]. For example, the high RON and low S of alkylate result in a modest merit value of 1.6, but the high RON and higher S of Premium-E10 fuel versus alkylate and Regular-E10 results in a merit value of 5.3 (Fig. 7, Table S4), corresponding to an expected 5.3% increase in engine efficiency. The product from Cu-Ni/BEA has a RON that is 1 unit greater than Premium-E10 with the same S, giving a slightly greater efficiency value of 5.9. The higher S values for the products from Cu/BEA (12) and Cu-Zn/BEA (14) result in markedly greater efficiency merit values of 7.5 and 9.7, respectively. These increased merit values over that of Premium-E10 suggest absolute engine efficiency gains of 2.3% (Cu/BEA) and 4.4% (Cu-Zn/BEA) compared to Premium-E10 if the product were used as an unblended fuel. If compared as a blendstock to alkylate, the products from Cu-Ni/BEA, Cu/BEA, and Cu-Zn/BEA provide engine efficiency gains of 4.3%, 5.9%, and 8.1% over that provided by alkylate. These increased merit values underscore the engine efficiency benefits that can be achieved by increasing S in a high RON mixture, rather than focusing solely on increasing RON.

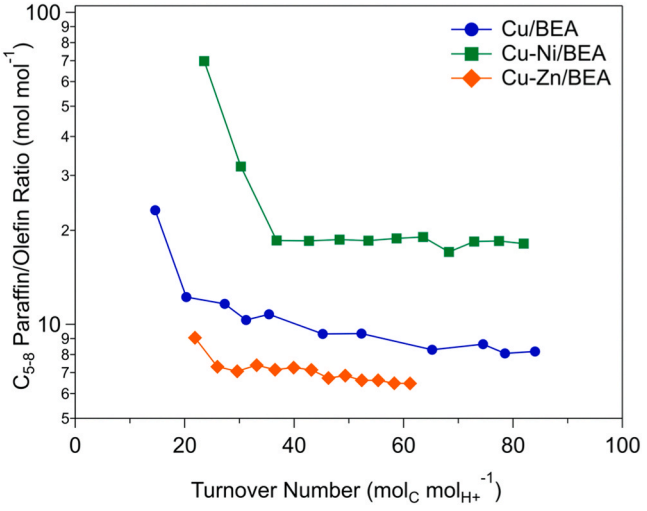

Fig. 6. Ratio of HOG paraffins-to-olefins from DME homologation over bimetallic Cu-M/BEA catalysts relative to benchmark Cu/BEA. Data are presented on log plot. Reaction conditions were 200 °C, 103 kPa, DME WHSV of ca. 2.2 h^{-1}, p_{DME} and p_{H2} each ca. 47 kPa, remainder p_{Ar}.

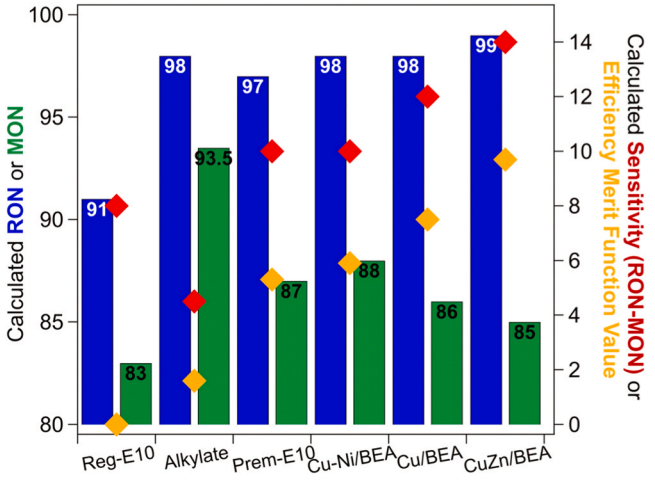

Fig. 7. Estimated fuel properties and expected engine efficiency for the C_{5-8} hydrocarbon products (RON, MON, S, and efficiency merit) over BEA catalysts compared to U.S. Regular-E10, Premium-E10 gasolines [19] and a representative refinery alkylate stream [40] ("Alkylate"). Data for BEA catalysts reported at TON = 52 ± 2 mol_C $mol_{H+}{}^{-1}$.

4. Conclusions

One approach to improve fuel economy is through increased fuel octane, since spark-ignition engines with reduced engine knock constraints can utilize high-octane fuels, ultimately reducing fleet fuel consumption [18,42]. Specifically, engine efficiency increases with higher RON and higher sensitivity fuels (S = difference in research and motor octane numbers) [16,17]. Here we demonstrated an advancement in an emerging and scalable catalytic pathway that converts renewable carbon sources to a high-RON hydrocarbon fuel by offering a means to adjust S, and thus engine efficiency, through targeted catalyst design to modify the net hydrogenation and dehydrogenation activity of multi-functional catalysts under the same reaction conditions. Informed by isobutane dehydrogenation reactions over ionic mono-metallic IE-M/BEA catalysts, bimetallic Cu-M/BEA catalysts were synthesized and characterized in depth to quantify the ionic and metallic species. During DME homologation, the Cu-Ni/BEA catalyst increased the HOG product P/O ratio to 19 mol mol^{-1} relative to benchmark Cu/BEA (9.4 mol mol^{-1}) due to the enhanced hydrogenation activity conferred by reduced metallic Ni species. In contrast, Cu-Zn/BEA provided a decrease in the P/O ratio to 6.6 mol mol^{-1} which was attributed to the enhanced net dehydrogenation activity from ionic Zn^{2+} sites and a greater total ionic site density.

The ability to adjust the P/O ratio, and thus the MON value, through catalyst design can be used to target high-S fuels that enable *high efficiency* engine operation. The MON value for the HOG product formed over Cu-Zn/BEA was reduced, and the resulting sensitivity of the fuel product was 14. Using a recently developed efficiency merit function to quantify the expected increase in engine efficiency compared to Regular-E10 gasoline (merit = 0), the HOG product from Cu-Zn/BEA exhibited a remarkably high value of 9.7 (Premium-E10 = 5.3, Cu/BEA = 7.5). This product could be used directly as a fuel or as a blendstock, similar to the manner in which alkylate streams are utilized in refining processes. Specifically, for Cu-Zn/BEA, the HOG product could be used as a high-RON blendstock that also increases the S of a finished gasoline fuel, and thus the expected engine efficiency. These results represent a foundational advancement in the catalytic pathway for DME to high-octane fuels using multi-functional BEA catalysts to access specific P/O ratios, and therefore specific fuel properties. Further tuning of the P/O ratio is envisioned with continued catalyst development to control active site densities in proportion to the desired activity (i.e., dehydrogenation versus hydrogenation).

CrediT authorship contribution statement

Connor P. Nash: Investigation, Formal analysis, Visualization, Writing – original draft **Daniel P. Dupuis:** Investigation, Formal analysis, Writing – original draft **Anurag Kumar:** Investigation, Formal analysis, Writing – review & editing **Carrie A. Farberow:** Investigation, Writing – review & editing **Anh T. To:** Investigation, Visualization, Writing – review & editing **Ce Yang:** Investigation, Data curation, Writing – review & editing **Evan C. Wegener:** Investigation, Formal analysis, Visualization, Writing – review & editing **Jeffrey T. Miller:** Formal analysis, Supervision, Writing – review & editing **Kinga A. Unocic:** Investigation, Visualization, Writing – review & editing **Earl Christensen:** Methodology, Writing – Original Draft **Jesse E. Hensley:** Supervision, Writing – Review & Editing **Joshua A. Schaidle:** Supervision, Writing – Review & Editing **Susan E. Habas:** Conceptualization, Supervision, Investigation, Writing – review & editing, Funding acquisition **Daniel A. Ruddy:** Conceptualization, Supervision, Investigation, Writing – review & editing, Funding acquisition.

Declaration of Competing Interest

The authors declare that they have no known competing financial interests or personal relationships that could have appeared to influence the work reported in this paper.

Acknowledgements

This work was authored in part by the National Renewable Energy Laboratory, operated by Alliance for Sustainable Energy, LLC, in part by Argonne National Laboratory, operated by The University of Chicago, and in part by Oak Ridge National Laboratory, operated by UT-Battelle, LLC, for the U.S. Department of Energy (DOE) under Contract Nos. DE-AC36-08GO28308, DE-AC02-06CH11357, and DE-AC05-00OR22725, respectively. Funding provided by the U.S. DOE Office of Energy Efficiency and Renewable Energy Bioenergy Technologies Office in collaboration with the Chemical Catalysis for Bioenergy (ChemCatBio) Consortium, a member of the Energy Materials Network (EMN). ECW and JTM were supported in part by the National Science Foundation under Cooperative Agreement No. EEC–1647722. This research used resources of the Advanced Photon Source, a U.S. DOE Office of Science User Facility operated for the DOE Office of Science by Argonne National Laboratory under Contract DE-AC02-06CH11357. MRCAT operations are supported by the Department of Energy and the MRCAT member institutions. The microscopy was performed as part of a user project at the Center for Nanophase Materials Sciences (CNMS), which is a U.S. DOE Office of Science User Facility. The views expressed in this article do not necessarily represent the views of the DOE or the U.S. Government. The U.S. Government retains and the publisher, by accepting the article for publication, acknowledges that the U.S. Government retains a nonexclusive, paid-up, irrevocable, worldwide license to publish or reproduce the published form of this work, or allow others to do so, for U.S. Government purposes.

Appendix A. Supporting information

Supplementary data associated with this article can be found in the online version at doi:10.1016/j.apcatb.2021.120801.

References

[1] EIA, January, Monthly Energy Review, U.S. Energy Information Administration, 2020.
[2] EIA, January, Monthly Energy Review, U.S. Energy Information Administration, 2020.
[3] EIA, Energy Consumption by Sector and Source, Annual Energy Outlook, U.S. Energy Information Administration, 2020.
[4] R.G. Grim, A.T. To, C.A. Farberow, J.E. Hensley, D.A. Ruddy, J.A. Schaidle, ACS Catal. 9 (2019) 4145–4172.
[5] J.H. Ahn, B. Temel, E. Iglesia, Angew. Chem. Int. Ed. 48 (2009) 3814–3816.
[6] D.A. Simonetti, J.H. Ahn, E. Iglesia, J. Catal. 277 (2011) 173–195.
[7] D.A. Simonetti, J.H. Ahn, E. Iglesia, ChemCatChem 3 (2011) 704–718.
[8] D.A. Simonetti, R.T. Carr, E. Iglesia, J. Catal. 285 (2012) 19–30.
[9] E.C.D. Tan, M. Talmadge, A. Dutta, J. Hensley, L.J. Snowden-Swan, D. Humbird, J. Schaidle, M. Biddy, Biofpr 10 (2016) 17–35.
[10] P. Ghosh, K.J. Hickey, S.B. Jaffe, Ind. Eng. Chem. Res. 45 (2006) 337–345.
[11] OPIS, The New Economics of Octane: What Drives the Cost of Octane and Why Octane Costs have Risen since 2012, (2017).
[12] J.A. Schaidle, D.A. Ruddy, S.E. Habas, M. Pan, G. Zhang, J.T. Miller, J.E. Hensley, ACS Catal. 5 (2015) 1794–1803.
[13] D.A. Ruddy, J.E. Hensley, C.P. Nash, E.C.D. Tan, E. Christensen, C.A. Farberow, F. G. Baddour, K.M. Van Allsburg, J.A. Schaidle, Nat. Catal. 2 (2019) 632–640.
[14] Q. Wu, A.T. To, C.P. Nash, D.P. Dupuis, F.G. Baddour, S.E. Habas, D.A. Ruddy, Appl. Catal. B: Environ. 287 (2021).
[15] C.K. Westbrook, M. Mehl, W.J. Pitz, M. Sjöberg, Combust. Flame 175 (2017) 2–15.
[16] G.T. Kalghatgi, SAE, (2001) Paper# 2001–2001-3584.
[17] G.T. Kalghatgi, SAE, (2001) Paper# 2001–2001-3585.
[18] R.L. Speth, E.W. Chow, R. Malina, S.R.H. Barrett, J.B. Heywood, W.H. Green, Environ. Sci. Technol. 48 (2014) 6561–6568.
[19] P. Miles, U.S. Department of Energy, Washington, D.C., 2018.
[20] I. Yarulina, K. De Wispelaere, S. Bailleul, J. Goetze, M. Radersma, E. Abou-Hamad, I. Vollmer, M. Goesten, B. Mezari, E.J.M. Hensen, J.S. Martinez-Espin, M. Morten, S. Mitchell, J. Perez-Ramirez, U. Olsbye, B.M. Weckhuysen, V. Van Speybroeck, F. Kapteijn, J. Gascon, Nat. Chem. 10 (2018) 804–812.
[21] S. Bailleul, I. Yarulina, A.E.J. Hoffman, A. Dokania, E. Abou-Hamad, A. D. Chowdhury, G. Pieters, J. Hajek, K. De Wispelaere, M. Waroquier, J. Gascon, V. Van Speybroeck, J. Am. Chem. Soc. 141 (2019) 14823–14842.
[22] X. Huo, N.A. Huq, J. Stunkel, N.S. Cleveland, A.K. Starace, A.E. Settle, A.M. York, R.S. Nelson, D.G. Brandner, L. Fouts, P.C. John St., E.D. Christensen, J. Luecke, J.

H. Mack, C.S. McEnally, P.A. Cherry, L.D. Pfefferle, T.J. Strathmann, D. Salvachúa, S. Kim, R.L. McCormick, G.T. Beckham, D.R. Vardon, Green. Chem. 21 (2019) 5813–5827.
[23] C.A. Farberow, S. Cheah, S. Kim, J.T. Miller, J.R. Gallagher, J.E. Hensley, J. A. Schaidle, D.A. Ruddy, ACS Catal. 7 (2017) 3662–3667.
[24] J. Camacho-Bunquin, P. Aich, M. Ferrandon, A. "Bean" Getsoian, U. Das, F. Dogan, L.A. Curtiss, J.T. Miller, C.L. Marshall, A.S. Hock, P.C. Stair, J. Catal. 345 (2017) 170–182.
[25] N.M. Schweitzer, B. Hu, U. Das, H. Kim, J. Greeley, L.A. Curtiss, P.C. Stair, J. T. Miller, A.S. Hock, ACS Catal. 4 (2014) 1091–1098.
[26] G. Zhang, C. Yang, J.T. Miller, ChemCatChem 10 (2018) 961–964.
[27] W.E. Farneth, R.J. Gorte, Chem. Rev. 95 (1995) 615–635.
[28] B. Ravel, M. Newville, J. Synchrotron Radiat. 12 (2005) 537–541.
[29] J.J. Rehr, J. de Mustre Leon, S.I. Zabinsky, R.C. Albers, J. Am. Chem. Soc. 113 (1991) 5135–5140.
[30] A. Hwang, D. Prieto-Centurion, A. Bhan, J. Catal. 337 (2016) 52–56.
[31] E.C.D. Tan, M. Talmadge, A. Dutta, J.E. Hensley, J.A. Schaidle, M. Biddy, D. Humbird, L.J. Snowden-Swan, J. Ross, D. Sexton, R. Yap, J. Lukas. NREL Technical Report, 2015, pp. 5100–62402.
[32] A. Kubacka, E. Wloch, B. Sulikowski, R.X. Valenzuela, V. Cortes-Corberan, Catal. Today 61 (2000) 343–352.
[33] Y. Ono, T. Baba, Phys. Chem. Chem. Phys. 17 (2015) 15637–15654.
[34] A.B. Getsoian, U. Das, J. Camacho-Bunquin, G. Zhang, J.R. Gallagher, B. Hu, S. Cheah, J.A. Schaidle, D.A. Ruddy, J.E. Hensley, T.R. Krause, L.A. Curtiss, J. T. Miller, A.S. Hock, Catal. Sci. Technol. 6 (2016) 6339–6353.
[35] G. Li, E.A. Pidko, ChemCatChem 11 (2018) 134–156.
[36] A. Dokania, A. Dutta Chowdhury, A. Ramirez, S. Telalovic, E. Abou-Hamad, L. Gevers, J. Ruiz-Martinez, J. Gascon, J. Catal. 381 (2020) 347–354.
[37] S. Ilias, A. Bhan, ACS Catal. 3 (2013) 18–31.
[38] S.S. Arora, D.L.S. Nieskens, A. Malek, A. Bhan, Nat. Catal. 1 (2018) 666–672.
[39] A. Demirbas, M.A. Balubaid, A.M. Basahel, W. Ahmad, M.H. Sheikh, Pet. Sci. Technol. 33 (2015) 1190–1197.
[40] P.R. Robinson, Petroleum Processing Overview, in: C.S. Hsu, P.R. Robinson (Eds.), Practical Advances in Petroleum Processing, Springer, New York, New York, NY, 2006, pp. 1–78.
[41] F.J. Keil, Micropor. Mesopor. Mat. 29 (1999) 49–66.
[42] E.W. Chow, J.B. Heywood, R.L. Speth, SAE Technical Papers, 1 (2014).